nature communications

Article

https://doi.org/10.1038/s41467-025-59225-z

Radiation-hardened dendritic-like nanocomposite films with ultrahigh capacitive energy density

Received: 11 January 2025

Accepted: 15 April 2025

Published online: 24 April 2025

Check for updates

Yajing Liu[1,8], Mengsha Li[2,8], Kai Jiang[3,8], Yang Zhang[1] ✉, Pin Gong[4], Sijia Song[1], Dong Li[1], Huan Liang[1], Xinmiao Huang[1], Jing Wang[5] ✉, Weiwei Li[1,6] ✉ & Ce-Wen Nan[7] ✉

Electrostatic dielectric capacitors are critical components in advanced electronic and electrical systems owing to their high-power density and ultrafast charge-discharge capability. However, achieving ultrahigh energy storage performance combined with robust radiation resistance remains a major challenge, particularly for practical applications in extreme environments. Guided by simulations, self-assembled nanocomposite films with dendritic-like structured ferroelectric embedded in an insulator are designed to overcome these challenges. This strategy boots energy storage performance by forming nano-polar regions and obstructing electric breakdown processes. More importantly, it not only exploits the intrinsic radiation-resistant properties of ferroelectric materials, but also takes advantages of abundant interfaces within the dendritic structure to enable a self-healing effect to improve radiation resistance. This self-healing mechanism, driven by interactions between ferroelectric and insulating phases, effectively eliminates radiation-induced defects and minimizes performance degradation under high radiation doses. Using this approach, we demonstrate the dendritic-like $PbZr_{0.53}Ti_{0.47}O_3$-MgO nanocomposite film capacitor exhibits an ultrahigh energy density over 200 joules per cubic centimeter and an excellent radiation tolerance exceeding 20 Mrad. This work offers a promising approach for the development of advanced electrostatic capacitors, particularly for applications in radiation-exposed power systems.

Energy storage dielectric capacitors are core components of high/pulsed power electronic devices, widely applied in fields such as hybrid electric vehicles, smart grids, and microwave communications, owing to their high-power density, ultrafast charge/discharge rates, and excellent reliability[1–7]. The primary parameters for evaluating energy storage performance of dielectric capacitors are recoverable energy density U_e and efficiency η, which are derived from the polarization-electric field (*P*-*E*) hysteresis loop by: $U_e = \int_{P_r}^{P_m} E dP$,

[1]College of Physics, MIIT Key Laboratory of Aerospace Information Materials and Physics, State Key Laboratory of Mechanics and Control for Aerospace Structures, Nanjing University of Aeronautics and Astronautics, Nanjing, China. [2]Center for Microscopy and Analysis, Nanjing University of Aeronautics and Astronautics, Nanjing, China. [3]School of Arts and Sciences, Shanghai Dianji University, Shanghai, China. [4]Department of Nuclear Science and Technology, Nanjing University of Aeronautics and Astronautics, Nanjing, China. [5]State Key Laboratory of Mechanics and Control for Aerospace Structures, College of Aerospace Engineering, Nanjing University of Aeronautics and Astronautics, Nanjing, China. [6]College of Integrated Circuits, MIIT Key Laboratory of Aerospace Integrated Circuits and Microsystem, Nanjing University of Aeronautics and Astronautics, Nanjing, China. [7]State Key Laboratory of New Ceramics and Fine Processing, School of Materials Science and Engineering, Tsinghua University, Beijing, China. [8]These authors contributed equally: Yajing Liu, Mengsha Li, Kai Jiang. ✉e-mail: zhangyang919@nuaa.edu.cn; wang-jing@nuaa.edu.cn; wl337@nuaa.edu.cn; cwnan@mail.tsinghua.cn

$\eta = [U_e/(U_e + U_{loss})] \times 100\%$ (Supplementary Fig. 1). Here, P_m and P_r represent maximum polarization and remnant polarization, respectively; U_{loss} refers to the energy loss caused by leakage or hysteresis, corresponding to the area inside the *P-E* loop (Supplementary Fig. 1). Therefore, achieving a large P_m, a small P_r, and a high breakdown field strength E_b is critical for optimizing both U_e and η. To quantitatively assess the balance between U_e and η, a figure of merit, $U_F = U_e/(1 - \eta)$ with an unit of J cm^{-3}, is often employed[3,8], where a higher value indicates better performance.

On the other hand, emerging technologies in extreme environments, including aerospace systems, nuclear energy, accelerator science, and radiation therapy technologies (e.g., nuclear imaging, radiotherapy, etc.)[9–11], demand dielectric capacitors that can withstand increasingly harsh operational conditions. A growing area of research addresses this challenge by studying the positive and negative effects of radiation on dielectric energy storage materials. Recent studies have shown that low-dose radiation (e.g., ion[6], electron[12], ultraviolet[13], and γ-ray[14]) can improve U_e in dielectrics, by inducing favorable defect complex, reducing leakage currents, and modifying defect structures. However, this positive effect often diminishes when exposed to high-doses radiation, which may attribute to the high density defect accumulation, structural degradation, and increased leakage currents. Consequently, a critical challenge is to understand the mechanisms of radiation-induced degradation and to develop novel strategies for designing higher-radiation-tolerant dielectric capacitors. Until now, there has been limited report on this aspect. It is particularly worth mentioning that γ-ray irradiation is the most wide radiation source existing in extreme environments[15]. Furthermore, commercially available dielectric capacitors suffer from relatively low energy storage density[16] and poor radiation tolerance (e.g., BOPP <10 Mrad)[17,18], restricting their potential for miniaturization and integration into advanced nanoelectronics in extreme environments. To address these challenges, it is imperative to develop next-generation dielectric capacitors that offer not only enhanced energy storage performance but also superior radiation resistance.

Ferroelectric (FE) oxide materials, such as $BaTiO_3$, $BiFeO_3$, and $PbZr_xTi_{1-x}O_3$, are one of attractive candidates for energy storage applications in radiation environments[19,20], owing to their large P_m and high radiation resistance. In previous reports, nanoelectronic devices based on these FE oxides, including ferroelectric random access memory[21,22] and piezoelectric sensors[23,24], have demonstrated resistance to radiation doses up to 10 Mrad[10,11,14,22,25]. However, FE oxides typically exhibit large P_r and low E_b, limiting their energy storage performance. Various strategies have been explored to overcome these limitations, such as domain engineering[2,3,26], artificial heterostructures[7,27–31], and defect design[6,32]. Despite these progresses, current strategies still face challenges, particularly the sacrificed P_m at their E_b. More than this, it should be emphasized that research on FE oxide-based capacitors targeting radiation-hardened energy storage systems remains largely unexplored.

Recently, nanocomposite materials with dendritic structure, featuring branching patterns and extensive interface regions, have been reported to effectively tailor a wide range of functionalities including conductivity[33], catalytic activity[34,35], and mechanical stability[36], benefiting from microscopic heterogeneities, interfacial bandgap/strain matching, specific crystallographic orientations, and extensive interface areas[37,38]. Thus, we propose that incorporating dendritic-like structure into FE-dielectric oxide nanocomposites may offer a promising approach to enhancing both dielectric energy performance and radiation resistance. In this configuration, the abundant tilted FE-dielectric interfaces can simultaneously reduce P_r and introduce relaxor properties by the formation of polar nano-regions (PNRs)[39–41], maintain P_m by preserving polar region connectivity, and enhance E_b by increasing electrical breakdown tortuosity. More importantly, these interfaces are well-established "defect sinks" that can absorb and annihilate radiation-induced defects[42,43], such as oxygen vacancies and interstitial atoms, thereby significantly improving radiation resistance[42–45]. Therefore, in this work, we design high-performance film capacitors starting from introducing a dendritic-like nano-polar (DNP) microstructure into self-assembled nanocomposite films composed of representative FE and dielectric/insulating materials, such as $PbZr_{0.53}Ti_{0.47}O_3$ (PZT) and MgO. PZT as the FE is chosen for its versatile phase structure[46], offering design flexibility for optimizing energy storage properties, while MgO as the insulator, with its wide bandgap (~ 7.8 eV)[47], effectively enhances breakdown strength compared to other insulators like ZnO (~ 3.4 eV)[48] and TiO_2 (~ 3.5 eV)[49]. By using this strategy, we achieve an ultrahigh energy density (217.8 J cm^{-3}), high efficiency (78%), remarkable radiation resistance (tolerating doses over 20 Mrad), excellent reliability (sustaining up to 10^{10} cycles), and impressive temperature stability (maintaining performance from −100 °C to 170 °C).

Results

Theoretical analyses of energy storage performance and self-healing mechanism

To evaluate the effectiveness of the DNP design in enhancing energy storage performance, we first conducted phase-field simulations to examine the dielectric breakdown and polarization switching processes for both plain PZT film and PZT-MgO (PM) film with DNP structures. The simulated PM film, consisting of a 50% PZT molar fraction, was generated by a simple dendritic crystal growth model[50] (Supplementary Fig. 2a). From the breakdown dynamics (Fig. 1a and Supplementary Fig. 3), we observed that the tortuous breakdown paths in the PM film split and diffuse at the interfaces between PZT and MgO phases, resulting in notably more complex pathways compared to the plain PZT film. Furthermore, the breakdown process in the PM film progresses more slowly (Supplementary Fig. 3), contributing to the enhancing E_b observed in subsequent experiments. In addition, the superior E_b of the PM film is also attributed to the disparity in bandgap values between PZT (ranging from 3.4 eV to 3.5 eV)[51,52] and MgO (7.8 eV)[47], which creates energy level mismatches at the interfaces, forming deep energy traps that hinder charge transport. These traps, combined with the ultralow leakage current (discussed later), reduce thermal stress and further prevent electric breakdown. The corresponding *P-E* loops for plain PZT and PM films under their acceptable applied electric fields are shown in Fig. 1b. The plain PZT film exbibits a typical squared *P-E* loop, characterized by noticeable hysteresis loss and high P_r at a relatively low electric field. By contrast, the *P-E* loop for the PM film is significantly slimmer, while maintaining high P_m at a higher electric field. Consequently, high energy storage density (indicated by the shaded areas of Fig. 1b) and efficiency can be achieved simultaneously in the PM films.

To understand the origin of large U_e in the PM films, we presented the evolution of local polarization configurations at different points in the *P-E* loop (Fig. 1c and Supplementary Fig. 2b). It should be noted that we incorporated charged point defects with certain concentration in the vicinity of the boundaries between the two phases, as such oxide nanocomposite film structures inevitably introduce numerous defects[53–56] (see Methods for detail). Initially (Panel 1, no electric field), the domain patterns appear disordered due to the present of boundaries and defects. Because of depolarization fields and gradient energy, the polarizations near these boundaries tend to align parallel to them. Meanwhile, the electric fields generated by charged defects cause the polarizations to orient towards or away from the defect sites, resulting in a pinning effect. When subjected to a large electric field (Panel 2), the polarizations generally align along the field direction, though they are still influenced by the boundaries and defects, particularly these nearby. Comparing Panel 1 and Panel 2, we found that the overall domain patterns remain largely unchanged. As the electric field

https://doi.org/10.1038/s41467-025-59225-z

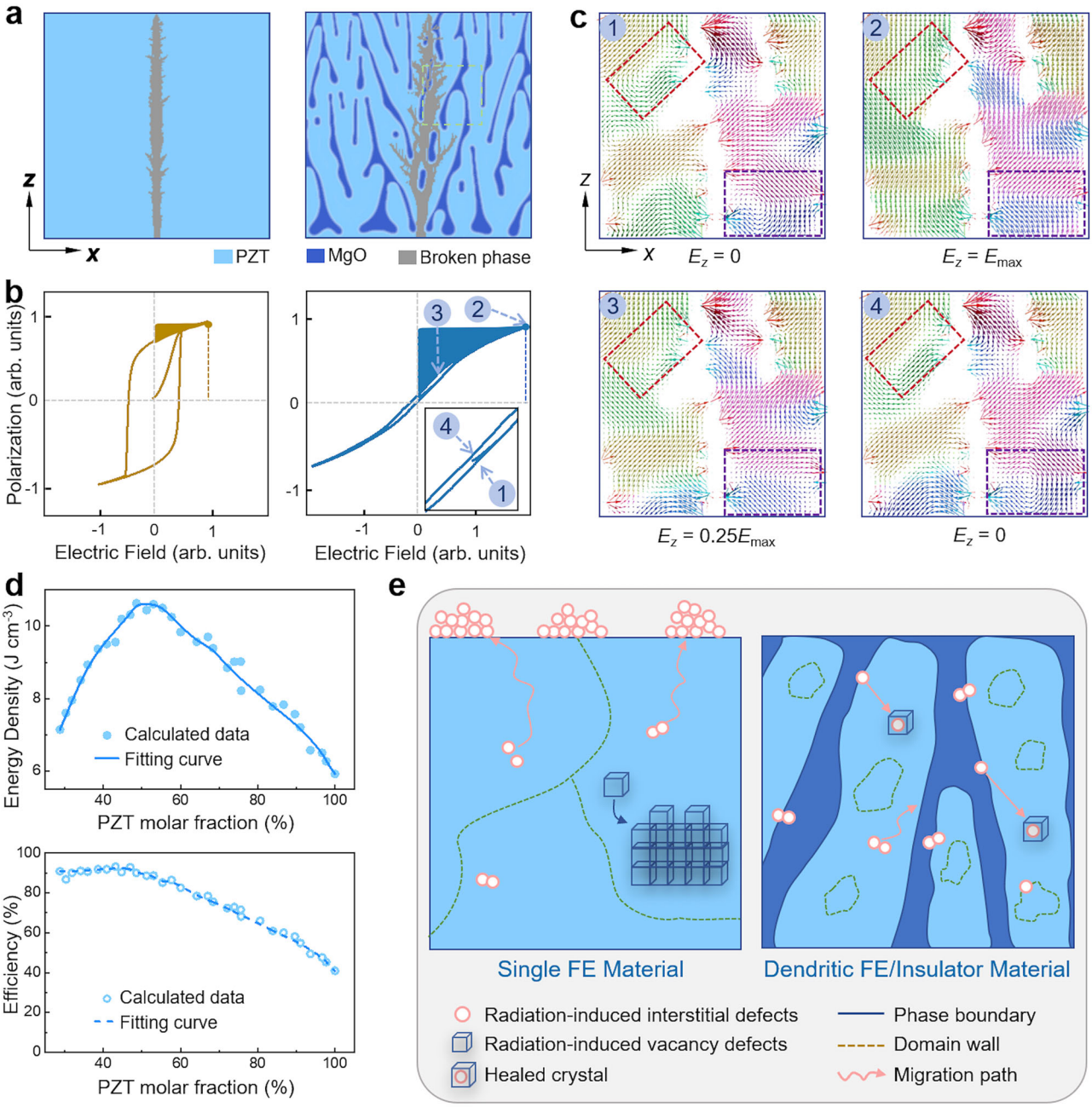

Fig. 1 | Design of self-assembled nanocomposite FEs with enhanced energy storage performance and radiation resistance. a, **b** Comparative display of breakdown paths and *P-E* loops for plain PZT and PM films, respectively. **c** Phase-field simulated local polarization distributions at various points in the *P-E* loop for the PM film, with arrows indicating the magnitude and directions of polarization at each site. The area shown is 18 nm × 18 nm. **d** Phase-field simulated energy density (top) and efficiency (down) of PM films as a function of PZT molar fractions at an electric field of 1 MV cm^{-1}. **e** Schematic illustration of possible self-healing evolution modes for conventional single FE material (left panel) and dendritic-like FE/dielectric nanocomposites with a high density of phase boundaries (right panel).

decreased (Panel 3 to 4), the pinned dipoles gradually return to their original states, thereby allowing the domain structures to revert to their initial configurations, which induces a small P_r and thus a large U_e. For comparison, we also simulated the same conditions for plain PZT film (Supplementary Fig. 4). In this case, the domain structure is permanently altered by the electric field, leading to a high P_r. In addition, we observed vortex-like domain structures in the PM film, as depicted by dashed rectangles in Fig. 1c. These domain patterns can be stabilized by the constraints imposed by defects and boundaries. Upon increasing and reducing the electric field, antiparallel domains disappear and then reappear, contributing to the antiferroelectric-like behavior observed in the *P-E* loop (Fig. 1b, right panel).

We further investigated the energy storage performance of the PM films across varying PZT fractions to identify the optimal composition (Fig. 1d). The plain PZT film, as anticipated, exhibits low U_e and η due to its squared *P-E* loop (Supplementary Fig. 4). Upon the incorporation of MgO, dendritic-like structures emerge (Supplementary Fig. 2), which introduce progressively more tortuous interfaces and enhanced pinning effects, leading to a significant reduction in P_r. Consequently, this enhances both U_e and η. However, when the PZT molar fraction drops below 50%, although P_r remains minimal, the excessive MgO content substantially diminishes P_m, resulting in a decline in U_e. Therefore, we found that high U_e values can be achieved with PZT molar fractions ranging from 45% to 60%, while η becomes

sufficiently high for fractions above 50%. These simulation results suggest that the optimal PZT molar fraction for enhanced energy storage performance may be around 50%.

Regarding the radiation resistance, radiation-induced degradation of FE properties is typically attributed to atom-displacement events and ionization effects, both of which are caused by increased defect concentrations[57,58]. Thus, the ability of a material to resist radiation damage is closely linked to the effectiveness of its microstructure in mitigating radiation-induced defects[43]. Grain boundaries and interphase interfaces have long been recognized as effective sinks for various types of defects[43]. For clarity in subsequent discussions, we use phase boundaries (PBs) to denote the interfaces between PZT and MgO. In single FE materials with limited domain walls (Fig. 1e, left panel), interstitial atoms migrate rapidly to the material surface, leaving vacancies within the lattice. These point defects can self-order and aggregate, forming obstacles to dislocation motion and leading to material hardening as well as a decline in overall properties[43]. By contrast, the DNP-structured PM films (Fig. 1e, right panel) feature a high density of PBs and domain walls, thereby positioning lattice atoms in close proximity to these interfaces. PBs are considered as the representative internal interfaces, while domain walls within the PZT phase may also contribute to the self-healing. These PBs can capture radiation-induced interstitial defects and subsequently release them back into lattice vacancies. Consequently, most vacancies can be restored to a healed crystal state within the annihilation range of these PBs, significantly enhancing radiation resistance of the DNP-structured PM films.

Fabrication and energy storage performance of dendritic-like self-assembled FE-dielectric nanocomposite film

Guided by phase-field simulations, we fabricated plain PZT film and a series of PZT_x-MgO_{1-x} (PM, $x = 0.65$, 0.5, and 0.35 representing the PZT molar fraction) nanocomposite film with a thickness of ~100 nm on $SrRuO_3$ (SRO)-buffered (001) $SrTiO_3$ (STO) single-crystalline substrates by pulsed laser deposition. High-angle annular dark-field scanning transmission electron microscopy (HAADF-STEM) images and X-ray diffraction (XRD) analysis demonstrate the formation of a distinct separation between PZT (light parts) and MgO (dark parts) phases in PM films. And the desired dendritic-like nanocomposite structure was successfully achieved in PM film with $x = 0.5$ (Supplementary Fig. 5). Energy-dispersive X-ray spectroscopy mapping (Supplementary Fig. 6) further revealed a uniform distribution of chemical elements, with a well-matched elemental ratio of Pb:Zr:Ti:Mg ≈ 1:0.53:0.47:1 in the PM film with $x = 0.5$ (Supplementary Table 1). The PZT exhibits a slightly reduction in lattice parameter of c/a after the incorporation of MgO (Supplementary Table 2), which may contribute to its relaxor behavior and, consequently, enhance its energy storage performance. For ease of discussion, "$P_{50}M_{50}$" is used to denote PM film with $x = 0.5$.

The dielectric permittivity of plain PZT and $P_{50}M_{50}$ film was measured as a function of temperature at a frequency of 100 kHz (Supplementary Fig. 7). For plain PZT film, the maximal-permittivity temperature T_m (phase-transition Curie temperature for typical FE) is ~355 °C, consistent with previous report[59]. Upon MgO incorporation, we observed a substantial decrease in T_m and a more diffused phase-transition peak, indicating enhanced relaxor properties induced by PNRs in the $P_{50}M_{50}$ film. This was further quantified by an increase in the relaxor diffuseness factor γ (derived from modified Cuire-Weiss law, Supplementary Fig. 7c, d) from 1.05 (for plain PZT film, similar to an ideal FE) to 1.88 (for the $P_{50}M_{50}$ film, similar to an ideal relaxor FE), with notably suppressed dielectric loss tangent over a wide range of temperature (from 25 °C to 400 °C) (Supplementary Fig. 7b)[4,5].

We then measured the *P-E* loops, a widely used method for evaluating the energy storage performance, of plain PZT film (1.0 MV cm^{-1}, nearly approaching its breakdown field) and $P_{50}M_{50}$ film (4.0 MV cm^{-1}) at a frequency of 1 kHz (Supplementary Fig. 8). The PZT film exhibits a typical square-shaped hysteresis with a large P_m of 67.1 μC cm^{-2} and a high P_r of 45.9 μC cm^{-2}, consistent with previous report[60], resulting in low U_e of 7.8 J cm^{-3} and η of 36.5% (Supplementary Fig. 8a). By contrast, the $P_{50}M_{50}$ film display relaxor-type slimmer *P-E* loops with a high P_m of 75.3 μC cm^{-2} and a remarkably low P_r of 6.5 μC cm^{-2}, resulting in a substantial P_m–P_r of 68.8 μC cm^{-2}. This large P_m–P_r value yields a high U_e of 99.0 J cm^{-3}, while simultaneously preserving an η of 78.2%, thereby indicating excellent energy storage performance (Supplementary Fig. 8b). The higher P_m in $P_{50}M_{50}$ film compared to PZT film is due to its significantly higher tolerance to de applied electric field. We also observed an obvious antiferroelectric-like phenomenon in the *P-E* loops near zero electric field in $P_{50}M_{50}$ film (Supplementary Fig. 8b), which may be linked to Mg^{2+} diffusion between MgO and PZT phases[61] and vortex-like domains, likely contributing to the improved energy storage performance, as discussed earlier in Fig. 1c. Overall, the $P_{50}M_{50}$ film, characterized by dendritic-like nanocomposite structure, demonstrates a significant enhancement in energy storage performance, which is attributed to its strong relaxor feature, high maximum polarization, and low remanent polarization. The relaxor behavior stems arises from the disordered rhombohedral and tetragonal nanodomains in PZT phase with size of 1 ~ 3 nm (Supplementary Fig. 9), which result from the disruption of long-range ferroelectric order in PZT phase by spatially distributed MgO phase and local lattice distortion caused by slight Mg^{2+} diffusion at MgO/PZT interfaces, leading to weakened domain intercoupling and reduced energy barriers for domain switching[2,3]. Furthermore, the smaller nanodomain size increases the number of domain walls, which, along with PBs, will benefit the film's radiation resistance. In addition, the energy storage performance of the $P_{50}M_{50}$ film exhibits excellent frequency stability with variation less than 3% (Supplementary Fig. 10). Overall, the $P_{50}M_{50}$ film with an optimized 100 nm thickness was selected for radiation resistance investigation due to its combined large U_e, high η, and high tolerance for electric field (Supplementary Fig. 8).

Radiation resistance in dendrite-like self-assembled FE-dielectric nanocomposite film

To assess the radiation resistance of the $P_{50}M_{50}$ films, we exposed them to a ^{60}Co gamma source radiation at doses of 0, 5, 10, 20, and 40 Mrad (equivalent Si dose) with a dose rate of ~0.801 Mrad(Si)/h. After exposure, XRD θ-2θ scans and X-ray reciprocal space maps show no observable shifts in the peak positions of PZT and MgO (Supplementary Figs. 11 and 12), indicating the robustness of crystal structure against radiation. We then measured *P-E* loops of the $P_{50}M_{50}$ films before and after radiation at an electric field of 4 MV cm^{-1} to characterize the polarization and energy storage performance (Fig. 2a). The variations in P_m, P_r, and $P_m - P_r$ values as a function of radiation doses are summarized in Fig. 2b. Notably, from 0 Mrad to 20 Mrad, P_m changes slightly (less than 2%), while P_r decreased significantly by 31%, resulting in an increased $P_m - P_r$ of 70.0 μC cm^{-2} for the 20 Mrad-irradiated $P_{50}M_{50}$ film. By contrast, when the dose is further increased to 40 Mrad, P_m decreases by 6%, P_r drops by 33.7%, and $P_m - P_r$ decreases to 64.8 μC cm^{-2}. We also observed a subtle rightward shift in the *P-E* loops from 5 Mrad to 40 Mrad (Fig. 2a), which is the primary factor contributing to the reduction of P_r. This shift and the degradation in polarization are likely attributed to the domain pinning effect induced by gamma-ray radiation.

The energy storage performance of the radiated $P_{50}M_{50}$ films was further assessed from their *P-E* loops (Fig. 2c). The pristine $P_{50}M_{50}$ film (i.e., 0 Mrad) shows a U_e of 99.0 J cm^{-3}, an η of 78%, and a high U_F of 450. As the radiation dose increases to 10 Mrad, the $P_{50}M_{50}$ film exhibits a slightly improved energy storage performance, with U_e rising to 100.8 J cm^{-3}, η remaining at 78%, and U_F to 458. This increase in U_e is attributed to the increased P_m, a common phenomenon observed in FE oxides upon exposure to low-dose radiation[11], likely due to the charging of internal interfaces induced by ionizing effect, thus

https://doi.org/10.1038/s41467-025-59225-z

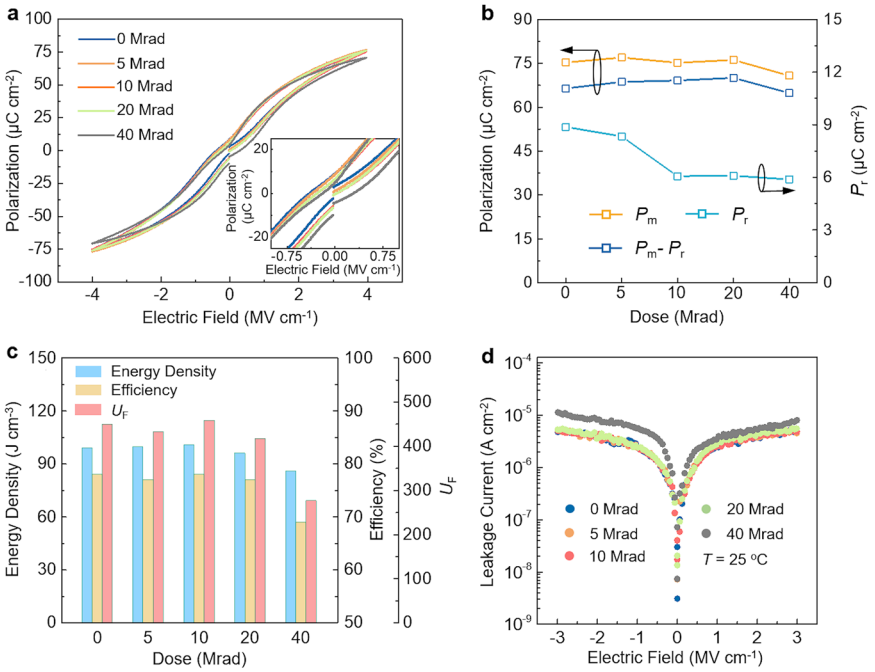

Fig. 2 | Ferroelectric and energy storage properties under different radiation doses. a *P-E* loops measured at 4.0 MV cm^{-1} and 1 kHz. **b** Variations of P_m, P_r, and P_m-P_r. **c** Comparison of energy density, efficiency, and U_F derived from (**a**). **d** Leakage current densities as a function of the applied electric field.

neutralizing pre-existing internal bias within films. Particularly, thanks to the abundant PBs characteristics, the radiation threshold for this "low dose" effect has been significantly increased from 2 Mrad, as reported in previous literature[11], to 20 Mrad in this work. At 20 Mrad, the $P_{50}M_{50}$ film still exhibits excellent energy storage performance, with U_e of 96.0 J cm^{-3}, η of 77%, and U_F of 417, comparable to the pristine $P_{50}M_{50}$ film (i.e., 0 Mrad). At 40 Mrad, however, the energy storage performance deteriorates significantly, with U_e dropping to 85.8 J cm^{-3}, η to 69%, and U_F to 276.7. This decline is attributed to the significant decrease in P_m from 76.2 μC cm^{-2} (20 Mrad) to 70.6 μC cm^{-2} (40 Mrad) (Fig. 2b) and the increase in leakage current from 5.3×10^{-6} A cm^{-2} (0 Mrad) to 1.2×10^{-5} A cm^{-2} (40 Mrad) (Fig. 2d). The increased leakage current at 40 Mrad is ascribed to the space-charge-limited conduction under high electric fields (Supplementary Fig. 13). In addition, the slight asymmetric leakage current at 40 Mrad may be attributed to the internal electric field caused by the accumulation of radiation-induced defects at electrode interfaces, which may affect charge transport differently under positive and negative bias. Therefore, as the radiation dose increases, U_e exhibits a trend of slight increase (≤ 10 Mrad) followed by a decrease (> 20 Mrad).

The mechanism of radiation effects on energy storage performance

Radiation-induced defects, including interstitial atoms and vacancies (most typically oxygen vacancies) from displacement effects and electron-hole pairs from ionizing effects, as well as their interactions, are the main factors contributing to the degradation of polarization switching in FE oxides[62,63]. As discussed earlier in Fig. 1e, PBs can act as sinks for these defects, healing vacancies to a healthy lattice and thereby enhancing the film's radiation resistance. To better understand the mechanisms of high radiation tolerance (≤ 20 Mrad) and degradation (40 Mrad) in macroscopic energy storage performance in the $P_{50}M_{50}$ films, we conducted detailed microstructure characterizations using PFM and STEM measurements (Fig. 3 and Supplementary Fig. 14). As shown in Fig. 3a and Supplementary Fig. 14a, the pristine $P_{50}M_{50}$ film (i.e., 0 Mrad) exhibits a homogeneous surface with a uniform typical FE switching butterfly shape in amplitude-voltage loops and nearly 180° reversal in phase-voltage loops across the tested 3 × 3 matrix (Fig. 3b and Supplementary Fig. 15). Such homogeneous surface remains stable even at radiation doses up to 10 Mrad (Supplementary Fig. 14c), ensuring its robust stability in energy storage performance. This stability may be attributed to the strong self-healing ability of the $P_{50}M_{50}$ film with DNP structure, which can effectively repair most radiation-induced defects. At a radiation dose of 20 Mrad, while most defects are restored to a healthy state, minor residual defects begin to accumulate and self-order near the film surface (Supplementary Fig. 14d), slightly hindering domain wall motion. Nevertheless, this effect is not significant enough to impact large-scale domain wall motion or the macroscopic performance, as confirmed by the results at radiation doses ≤ 20 Mrad (Fig. 2).

However, at 40 Mrad, numerous defect clusters appear on the film surface (highlighted by pink circles in Fig. 3c and Supplementary Fig. 14e). Compared to the non-clustered regions (represented by blue circles in Fig. 3c), these clustered regions (represented by pink circles, such as domain 2 in Fig. 3c) exhibit a decreased piezoelectric response by approximately 60% and non-180° reversal (Fig. 3d and Supplementary Fig. 16), which eventually leads to the obvious degradation in the macroscopic energy storage performance (Fig. 2). Defects and dislocations are inevitable during the fabrication of complex oxide films[53,55,64], and the pre-existing dislocations were identified at PBs in the pristine $P_{50}M_{50}$ film (i.e., 0 Mrad, Fig. 3e, f). After irradiated by an ultrahigh dose (40 Mrad), a large population of mobile defects cannot be healed back to a healthy state, accumulating and self-ordering at PBs and film surface, ultimately resulting in additional misfit dislocations at PBs (Fig. 3g, h) and clusters on the film surface (Fig. 3c). In addition, ionization effects generate a large number of electron-hole pairs[11], migrating to PBs and film surface, where they are trapped by dislocations beneath PBs. This trapping creates an internal bias, inducing domain pinning effect as observed in Fig. 3d, which explains the rightward shift of *P-E* loops and the attenuation of P_m in the 40 Mrad-irradiated $P_{50}M_{50}$ film (Fig. 2a). These findings suggest that the degradation in macroscopic energy storage performance at 40 Mrad may originate from the domain pinning effects induced by radiation. This align with previous studies on radiation-induced degradation of

https://doi.org/10.1038/s41467-025-59225-z

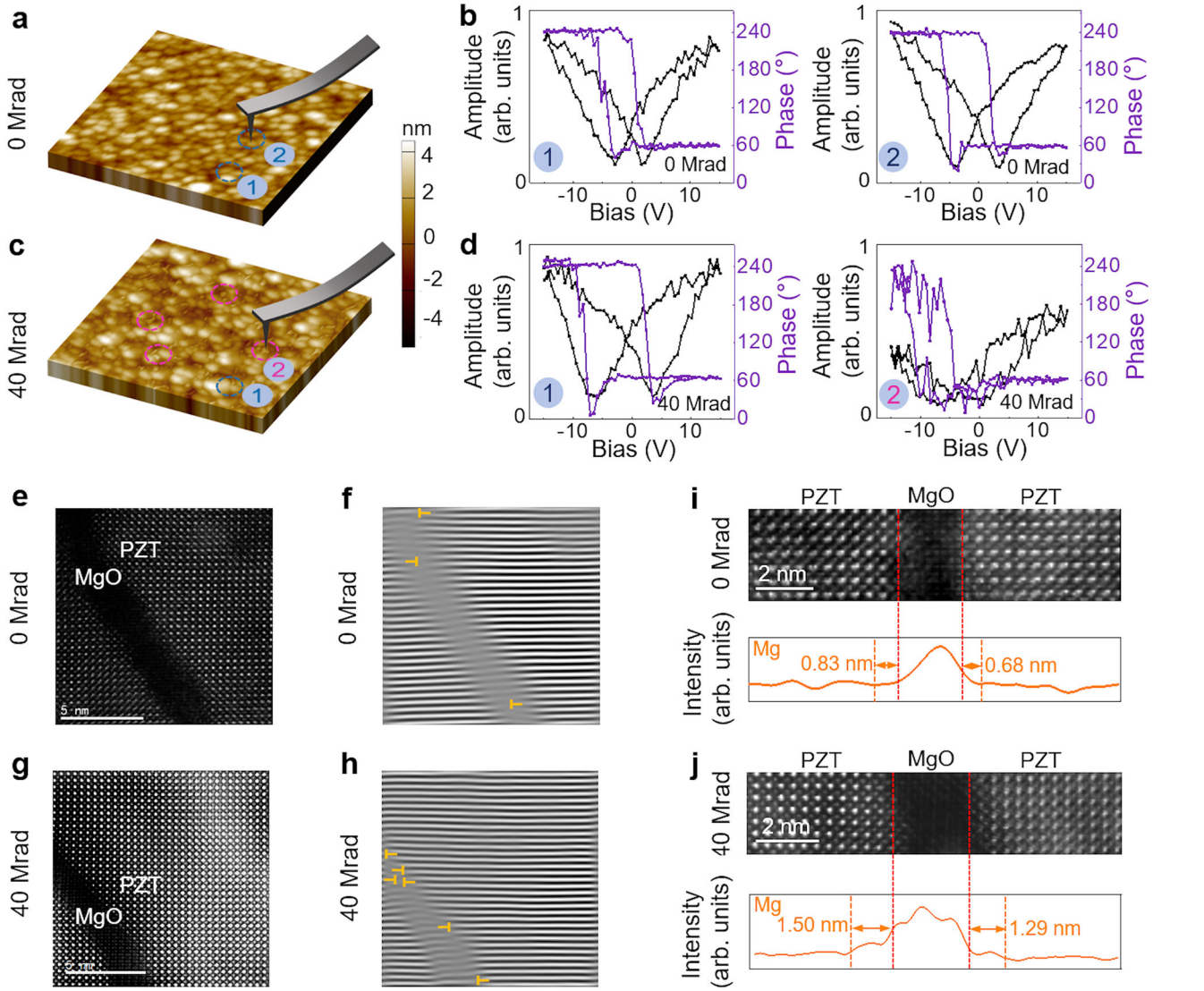

Fig. 3 | Microstructure analysis. AFM images with a range of 2 × 2 μm (**a**, **c**), local amplitude and phase hysteresis loops from (**a**, **c**) selected area (**b**, **d**), HAADF-STEM images (**e**, **g**), inverse Fast Fourier-filtered (FFT) images (**f**, **h**), and Mg intensity line profiles across PZT/MgO boundaries (**i**, **j**) for 0 Mrad and 40 Mrad irradiated $P_{50}M_{50}$ films, respectively.

domain wall motion in FE oxide films[22,65]. Moreover, compared to the pristine $P_{50}M_{50}$ film (i.e., 0 Mrad, Fig. 3i), the $P_{50}M_{50}$ film exposed to 40 Mrad shows an increased diffusion of Mg^{2+} across PBs (Fig. 3j), which may further strengthen the domain pinning effect.

Radiation effects on comprehensively energy storage performance

To comprehensively explore the radiation effects on the energy storage performance of the $P_{50}M_{50}$ films, we assessed their statistical breakdown strengths E_b using Weibull distribution fitting (Fig. 4a). The pristine $P_{50}M_{50}$ film (i.e., 0 Mrad) exhibits an ultrahigh E_b of 7.1 MV cm^{-1}, surpassing those of most existing state-of-the-art dielectric oxide films[3–7,27], such as 5.3 MV cm^{-1} in Sm-$BiFeO_3$-$BaTiO_3$ films[3], 5.6 MV cm^{-1} in MoS_2/$BaTiO_3$/MoS_2 heterostructures[7], 5.9 MV cm^{-1} in ion-irradiated $Pb(Mg_{1/3}Nb_{2/3})O_3$-$PbTiO_3$ films[6], 6.35 MV cm^{-1} in $(Bi_{3.25}La_{0.75})(Ti_{3-3x}Zr_xHf_xSn_x)O_{12}$ films[4], and 7.0 MV cm^{-1} in $Bi(Mg_{0.5}Ti_{0.5})O_3$-$SrTiO_3$ films[27]. After exposure to 20 Mrad, the $P_{50}M_{50}$ film still maintains an E_b of 6.8 MV cm^{-1}, comparable to that of the pristine $P_{50}M_{50}$ film. At 40 Mrad, however, E_b decreases to 6.5 MV cm^{-1}, accompanied by a diminished β value to 11.7, suggesting a reduction in the reliability of E_b data.

We then evaluated U_e and η from the bipolar *P-E* loops at electric fields up to their respective E_b and at a frequency of 1 kHz (Fig. 4b and Supplementary Fig. 17). The pristine $P_{50}M_{50}$ film (i.e., 0 Mrad) achieves an exceptional U_e of 217.8 J cm^{-3}, η of ~ 78%, and U_F of 990, owing to the large $P_m - P_r$ (90.7 μC cm^{-2}) and ultrahigh E_b (7.1 MV cm^{-1}). These values outperform the best lead-free and lead-based dielectric oxide films (Fig. 4c)[2–6,14,27,29,66,67]. After exposure to 20 Mrad, the $P_{50}M_{50}$ film still retains an excellent energy storage performance with U_e of 197.8 μC cm^{-2}, η of 76.1%, and U_F of 828, maintaining competitive (Fig. 4c). By contrast, at 40 Mrad, marked reductions in both U_e (156.9 μC cm^{-2}), η (68.8%), and U_F (503) are observed due to the reduced $P_m - P_r$ and E_b, and the increased leakage current (Fig. 2).

For practical dielectric capacitor applications, we further evaluated the reliability and temperature stability of the $P_{50}M_{50}$ films by varying radiation doses (Fig. 4d, e and Supplementary Figs. 18 and 19). A triangle electric field of 4 MV cm^{-1} was applied during accelerated charge-discharge tests. We found that the $P_{50}M_{50}$ film exhibits robust reliability against fatigue with radiation doses up to 20 Mrad. For instance, compared to the pristine $P_{50}M_{50}$ film (i.e., 0 Mrad, $\Delta U_e \leq 8\%$, $\Delta\eta \leq 8\%$), the 20 Mrad-irradiated film sustains over 10^{10} cycles, with minimal degradation of U_e ($\Delta U_e \leq 8.9\%$) and η ($\Delta\eta \leq 3.6\%$) (Fig. 4d). By

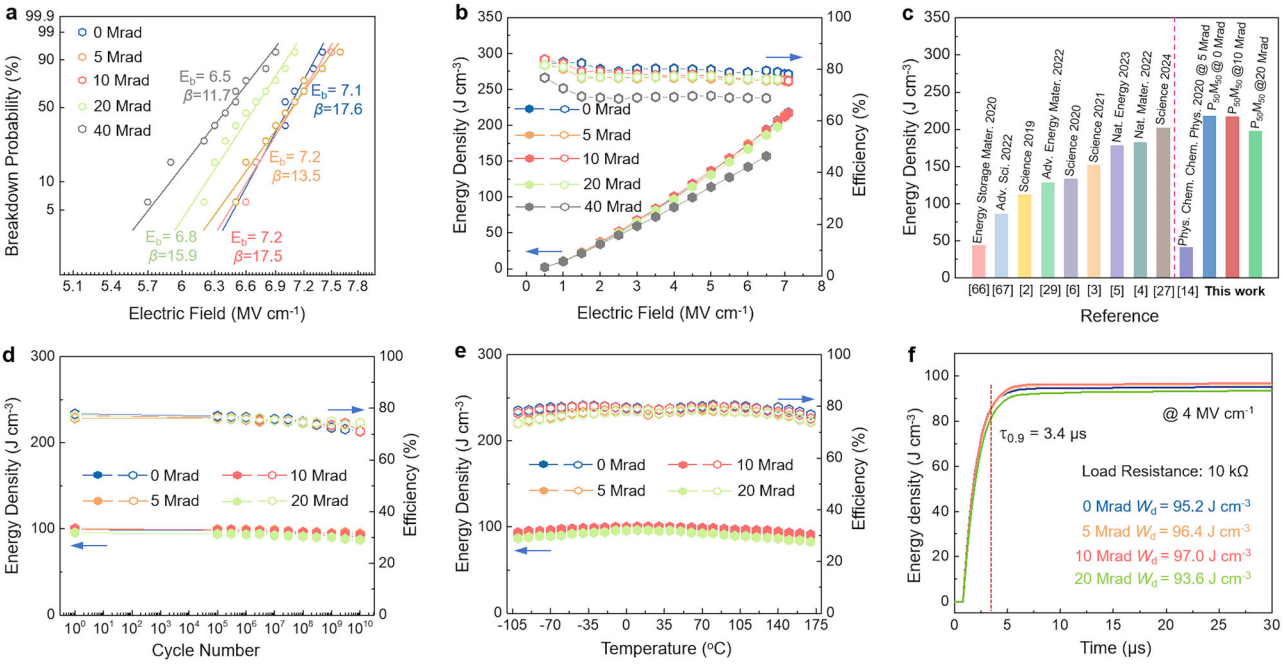

Fig. 4 | Energy storage performance under radiation exposure. a Weibull distribution analysis of characteristic breakdown fields. **b** Energy density and efficiency at electric fields up to their E_b. **c** Comparison of energy density of the $P_{50}M_{50}$ films with the state-of-the-art dielectric films. **d** Charging-discharging reliability of energy storage performance at an electric field of 4 MV cm^{-1}. **e** Temperature dependence of energy storage performances at an electric field of 4 MV cm^{-1} over a temperature range from −100 °C to 170 °C. **f** Discharge energy density as a function of time measured at different electric fields.

contrast, at 40 Mrad, a sharp decline is observed in both U_e (ΔU_e ~ 34%) and η (Δη ~ 22%) after 3×10^5 cycles (Supplementary Fig. 20a), likely due to the high density of radiation-induced defects including oxygen vacancies, interstitial atoms, and their clusters[9,20,22] (Fig. 3c, h, and j). In addition, we noticed that the antiferroelectric-like behavior gradually disappeared in the 40 Mrad irradiated $P_{50}M_{50}$ film (Supplementary Fig. 18e), which may be caused by cumulative irradiation damage during fatigue cycling. This damage disrupts the vortex-like domains, thereby destabilizing the antiferroelectric dipolar ordering.

In addition, the $P_{50}M_{50}$ films also demonstrate exceptional thermal stability, with slight variations from 0 Mrad ($\Delta U_e \le 3.1\%$, $\Delta\eta \le 2\%$) to 20 Mrad ($\Delta U_e \le 4.5\%$, $\Delta\eta \le 5\%$) across a broad temperature range from −100 °C to 170 °C (Fig. 4e). The remarkable thermal stability is attributed to the robust relaxor properties, i.e., the dielectric permittivity remains unaffected by temperature variations, even at radiation dose of 20 Mrad (Supplementary Fig. 21). This superior thermal stability enables the $P_{50}M_{50}$ film to function normally even under multiple harsh conditions such as high radiation and high temperature. However, at 40 Mrad, the $P_{50}M_{50}$ film shows a relatively lower U_e from −100 °C to 130 °C and undergoes breakdown at temperatures exceeding 130 °C (Supplementary Fig. 20b). We also measured the overdamped discharge at 4 MV cm^{-1} with a load resistor of 10 kΩ (Supplementary Fig. 22). An ultrahigh discharge energy density (W_d) and a fast discharge rate ($\tau_{0.9}$) are obtained at both 0 Mrad (W_d ~ 95.2 J cm^{-3}, $\tau_{0.9}$ ~ 3.4 μs) and 20 Mrad (W_d ~ 93.6 J cm^{-3}, $\tau_{0.9}$ ~ 3.4 μs) (Fig. 4f). These results, together with ultrahigh energy storage performance and radiation tolerance (over 20 Mrad), excellent temperature stability (−100 to 170 °C), and reliability (over 10^{10} cycles), highlight the promising charge-discharge performance of the $P_{50}M_{50}$ film in radiation environments, making it a potential candidate for pulsed-power applications, particularly under extreme conditions.

Discussion

In summary, we proposed a DNP structure in self-assembled FE-dielectric nanocomposite films, incorporating numerous phase boundaries and domain walls, to simultaneously enhance both energy storage performance and radiation resistance. The DNP structure-designed film capacitors achieve an ultrahigh energy density of 217.8 J cm^{-3} and an efficiency of 78%. More importantly, the phase boundaries and domain walls within the films effectively improve the radiation tolerance, temperature stability, and reliability, making them suitable for applications in spacecraft and satellite power systems, portable medical pulsed power systems, and harsh-environment industrial electronics. This work provides a strategy for developing high-performance and radiation-resistant energy storage capacitors. Future work should extend our DNP strategy to other lead-free ferroelectric-insulator composites, such as $BiFeO_3$-based, $BaTiO_3$-based, and HfO_2-ZrO_2 binary oxides[68,69], to develop environmentally friendly energy storage devices.

Methods

Fabrication of the film

High-quality $PbZr_{0.53}Ti_{0.47}O_3$ (PZT) and $(PbZr_{0.53}Ti_{0.47}O_3)_{0.5}$–$MgO_{0.5}$ ($P_{50}M_{50}$) thin films were grown on (001) $SrRuO_3$ (SRO) buffered $SrTiO_3$ (STO) substrates by pulsed laser deposition with a KrF laser (λ = 248 nm) under 4 Hz and 1.23 J cm^{-2}. Prior to the growth of PZT and $P_{50}M_{50}$ layer, the SRO buffer layer was deposited at a substrate temperature of 630 °C under an oxygen partial pressure of 0.15 mbar. The PZT and $P_{50}M_{50}$ films were fabricated by the growth temperature of 510 °C and the oxygen pressure of 0.15 mbar, and then annealed for 20 min under the same temperature and oxygen pressure before being cooled down to room temperature. Sputtered Pt top electrodes with an area of 1.962×10^{-5} cm^2 were used for electrical measurement.

The $P_{50}M_{50}$ films were adhered to a Printed Circuit Board and then exposed to ^{60}Co-gamma radiation with doses of 5, 10, 20, and 40 Mrad(Si) at a rate of 0.801 Mrad(Si)/h. The incident direction of γ-ray was set to 90° from the film surface using an open circuit state for devices during the radiation. High vacuum condition was used to store all films after γ-ray irradiation.

Structural characterizations

The crystal structures and surface morphologies of the films were analyzed by high-resolution four-circle XRD (Panalytical Empyrean, K_α

radiation, $\lambda = 1.5405$ Å) and atomic force microscopy (AFM, Asylum Research MFP-3D), respectively.

Physical properties characterizations

Radiant Precision materials analyzer was used for ferroelectric hysteresis loops, current-voltage curves, and fatigue endurance measurements. The dielectric and piezoresponse force microscopy (PFM) measurements were conducted by an Impedance Analyzer (EA990A) and Asylum Research MFP-3D origin with an HVA 220 high-voltage amplifier, respectively.

Scanning transmission electron microscopy

Cross-sectional TEM specimens oriented along the $[100]_{pc}$ direction were prepared by an focused ion beam system (FEI Versa3D) with 30 kV Ga ions, followed by a low-voltage cleaning step. STEM studies were performed using a double aberration-corrected STEM (Thermo Fisher Scientific Spectra 300) equipped with a cold-field emission gun and Cs CETCOR/S-CORR double correctors operated at 300 kV. The HAADF-STEM images were obtained using an estimated probe current of 27 pA. The convergence and collection semi-angles were 25 and 49–200 mrad. The positions of the Pb and Ti (Zr) atomic columns were precisely determined using an iterative center-of-mass peak finding method. These coordinates were then used to calculate the cationic displacements of Ti^{4+} (Zr^{4+}) relative to the centers of the nearest neighboring Pb^{2+} ions.

Phase-field simulation for dielectric breakdown

To simulate the dielectric breakdown process, we utilized a phase-field model that introduces a continuous variable $\eta(\mathbf{r}, t)$ to characterize the breakdown phase[70]. In this model, $\eta = 1$ indicates the broken regions, $\eta = 0$ indicates the non-broken regions, and $0 < \eta < 1$ represents the interface between two phases. The total free energy, including the phase separation term f_{sepa}, the gradient term f_{grad}, and the electrostatic term f_{elec}, can be written as

$$F = \int_V (f_{\text{sepa}} + f_{\text{grad}} + f_{\text{elec}}) \mathrm{d}V. \tag{1}$$

The phase separation energy density is described by a double-well function,

$$f_{\text{sepa}} = \alpha \eta^2 (1 - \eta)^2, \tag{2}$$

where α is a positive coefficient.

The gradient energy density is defined by

$$f_{\text{grad}} = \frac{1}{2} \gamma |\nabla \eta|^2, \tag{3}$$

where γ is the gradient energy coefficient.

The electrostatic energy density is expressed as

$$f_{\text{elec}} = -\frac{1}{2} \varepsilon_0 \varepsilon_r E_i E_i, \tag{4}$$

where ε_0 is the vacuum dielectric constant, ε_r is the position-dependent relative dielectric constant, and E_i is the electric field which can be calculated by a spectral iterative perturbation method[71]. The Einstein notation is used.

To model the evolution of the dielectric breakdown process, a modified Allen-Cahn equation is used,

$$\frac{\partial \eta(\mathbf{r}, t)}{\partial t} = -L_0 H(|f_{\text{elec}}| - |f_{\text{crit}}|) \frac{\delta F}{\delta \eta(\mathbf{r}, t)}, \tag{5}$$

where L_0 is the kinetic coefficient, $f_{\text{crit}} = 1/2 \varepsilon_0 \varepsilon_r E_b^2$ is a position-dependent constant indicating the maximal energy endurance with E_b as the position-related breakdown strength, and $H(|f_{\text{elec}}| - |f_{\text{crit}}|)$ is the Heaviside unit step function with $H(|f_{\text{elec}}| - |f_{\text{crit}}| > 0) = 1$ and $H(|f_{\text{elec}}| - |f_{\text{crit}}| < 0) = 0$.

In our simulations, $\alpha = 10^8$ J m^{-3}, $\gamma = 10^{-10}$ J m^{-1}, and $L_0 = 1/(t_0 \alpha)$ with t_0 as the characteristic time scale. The broken PM film is considered as a mixture of PZT, MgO, and broken regions. The position dependent $\varepsilon_r = 10^1$, 10^3, and 10^5 for MgO, PZT, and broken regions, respectively. The position dependent $E_b = 10$ MV cm^{-1} and 1.5 MV cm^{-1} for MgO and PZT regions, respectively. The whole system grid is $200\Delta x \times 1\Delta x \times 200\Delta x$ with $\Delta x = 0.4$ nm.

Phase-field simulation for polarization evolution

To simulate the polarization evolution of plain PZT and PM films, we employed a phase-field model where the polarization vector P_i ($i = 1, 2, 3$) was chosen as the order parameter. The total free energy, including the Landau free energy term f_{Land}, the gradient energy term f_{grad}, the elastic energy term f_{elas}, and the electrostatic energy term f_{elec}, is expressed as[72]

$$F = \int_V (f_{\text{Land}} + f_{\text{grad}} + f_{\text{elas}} + f_{\text{elec}}) \mathrm{d}V. \tag{6}$$

The Landau free energy density is

$$\begin{aligned} f_{\text{Land}} = {} & \alpha_1 (P_1^2 + P_2^2 + P_3^2) + \alpha_{11} (P_1^4 + P_2^4 + P_3^4) \\ & + \alpha_{12} (P_1^2 P_2^2 + P_2^2 P_3^2 + P_3^2 P_1^2) + \alpha_{111} (P_1^6 + P_2^6 + P_3^6) \\ & + \alpha_{12} [P_1^2 (P_2^4 + P_3^4) + P_2^2 (P_3^4 + P_1^4) + P_3^2 (P_1^4 + P_2^4)] \\ & + \alpha_{123} P_1^2 P_2^2 P_3^2, \end{aligned} \tag{7}$$

where α_1, α_{11}, α_{12}, α_{111}, α_{112}, and α_{123} are the Landau polynomial coefficients.

The gradient energy density is

$$\begin{aligned} f_{\text{grad}} = {} & \frac{1}{2} G_{11} (P_{1,1}^2 + P_{2,2}^2 + P_{3,3}^2) + G_{12} (P_{1,1} P_{2,2} + P_{2,2} P_{3,3} + P_{3,3} P_{1,1}) \\ & + \frac{1}{2} G_{44} [(P_{1,2} + P_{2,1})^2 + (P_{2,3} + P_{3,2})^2 + (P_{3,1} + P_{1,3})^2] \\ & + \frac{1}{2} G'_{44} [(P_{1,2} - P_{2,1})^2 + (P_{2,3} - P_{3,2})^2 + (P_{3,1} - P_{1,3})^2], \end{aligned} \tag{8}$$

where G_{11}, G_{12}, G_{44}, and G'_{44} are the gradient energy density coefficients, and $P_{i,j}$ denotes $\partial P_i / \partial x_j$ with x_j as the spatial coordinate.

The elastic energy density is

$$f_{\text{elas}} = \frac{1}{2} c_{ijkl} (\varepsilon_{ij} - \varepsilon_{ij}^0)(\varepsilon_{kl} - \varepsilon_{kl}^0), \tag{9}$$

where c_{ijkl} is the elastic stiffness tensor, ε_{ij} is the total strain, and $\varepsilon^0_{ij} = Q_{ijkl} P_k P_l$ is the eigenstrain with Q_{ijkl} as the electrostrictive coefficients. The Einstein notation is used.

The electrostatic energy density is

$$f_{\text{elec}} = -E_i P_i - \frac{1}{2} \varepsilon_0 \kappa_b E_i E_i, \tag{10}$$

where $E_i = -\partial \varphi / \partial x_i$ is the electric field with φ as the electrostatic potential, ε_0 is the permittivity of vacuum, and κ_b is the background relative dielectric constant.

The temporal evolution of order parameters was simulated by the time-dependent Ginzburg-Landau equations using the semi-implicit

Fourier spectral method[73]

$$\frac{\partial P_i}{\partial t} = -L_P \frac{\delta F}{\delta P}, \tag{11}$$

where L_P is the kinetic coefficient. For each time step, the elastic and electric driving forces were calculated by solving the mechanical equilibrium equations $\sigma_{ij,j} = 0$ and the electrostatic equilibrium equation $D_{i,i} = 0$, where $\sigma_{ij} = c_{ijkl}(\varepsilon_{ij} - \varepsilon^0_{ij})$ is the local stress and $D_i = \varepsilon_0 \kappa_b E_i + P_i$ is the electric displacement.

The PM systems can be considered as a mixture of PZT regions, MgO regions, and boundary regions, distinguished by the coefficients. For PZT, according to previous literatures[74,75], $\alpha_1 = 1.583 \times 10^5 \times (T - 657)$ $C^{-2}m^2N$ with $T = 300$ (in Kelvin) as the ambient temperature, $\alpha_{11} = 6.680 \times 10^7\, C^{-4}m^6N$, $\alpha_{12} = 1.944 \times 10^8\, C^{-4}m^6N$, $\alpha_{111} = 1.660 \times 10^8\, C^{-6}m^{10}N$, $\alpha_{112} = 7.576 \times 10^8\, C^{-6}m^{10}N$, $\alpha_{123} = -3.570 \times 10^9\, C^{-6}m^{10}N$, $c_{11} = 154$ GPa, $c_{12} = 84$ GPa, $c_{44} = 35$ GPa, and $\kappa_b = 40$. For MgO, $\alpha_1 = 5.650 \times 10^9\, C^{-2}m^2N$, $\alpha_{11} = \alpha_{12} = \alpha_{111} = \alpha_{112} = \alpha_{123} = 0$, $c_{11} = 293$ GPa, $c_{12} = 92$ GPa, $c_{44} = 155$ GPa, and $\kappa_b = 10$. For boundaries between PZT and MgO, the coefficients are the average of these of PZT and MgO. The spectral iterative perturbation method is used[71]. Meanwhile, for the gradient energy density coefficients, $G_{11} = 0.6G_{110}$, $G_{12} = 0$, and $G_{44} = G'_{44} = 0.3G_{110}$, where $G_{110} = 5.658 \times 10^{-11}\, C^{-2}m^4N$. For the electrostrictive coefficients, $Q_{11} = 0.09080\, C^{-2}m^4$, $Q_{12} = -0.04158\, C^{-2}m^4$, $Q_{44} = 0.07741\, C^{-2}m^4$.

The whole system grid is $500\Delta x \times 1\Delta x \times 400\Delta x$ with $\Delta x = 0.4$ nm, including 100 layers for substrate and 260 layers for the PM film, as illustrated in Supplementary Fig. 2a. The film boundary conditions were solved by a superposition method[76,77]. The closed-circuit electric boundary conditions were adopted.

To simulate the pinning effect of defects, we randomly added point charges in the boundary regions. The charges obey a normal distribution of mean $\mu = \pm\ 5.0 \times 10^9\, C/m^3$ (~2 e/u.c.) and standard deviation $\sigma = 0.1\mu$.

Data availability

All the experimental/calculation data that support the findings of this study are available from the corresponding authors upon request.

Code availability

All the codes used for this study are available from the corresponding authors upon request.

References

1. Li, Q. et al. Flexible high-temperature dielectric materials from polymer nanocomposites. *Nature* **523**, 576–579 (2015).
2. Pan, H. et al. Ultrahigh–energy density lead-free dielectric films via polymorphic nanodomain design. *Science* **365**, 578–582 (2019).
3. Pan, H. et al. Ultrahigh energy storage in superparaelectric relaxor ferroelectrics. *Science* **374**, 100–104 (2021).
4. Yang, B. et al. High-entropy enhanced capacitive energy storage. *Nat. Mater.* **21**, 1074–1080 (2022).
5. Yang, B. et al. Engineering relaxors by entropy for high energy storage performance. *Nat. Energy* **8**, 956–964 (2023).
6. Kim, J. et al. Ultrahigh capacitive energy density in ion-bombarded relaxor ferroelectric films. *Science* **369**, 81–84 (2020).
7. Han, S. et al. High energy density in artificial heterostructures through relaxation time modulation. *Science* **384**, 312–317 (2024).
8. Zhang, M. et al. Ultrahigh energy storage in high-entropy ceramic capacitors with polymorphic relaxor phase. *Science* **384**, 185–189 (2024).
9. Bogaerts, J. et al. Total dose and displacement damage effects in a radiation-hardened CMOS APS. *IEEE T. Electron Dev.* **50**, 84–90 (2003).
10. Brewer, S. J. et al. Effect of top electrode material on radiation-induced degradation of ferroelectric thin film structures. *J. Appl. Phys.* **120**, 024101 (2016).
11. Brewer, S. et al. Effects of crystallization interfaces on irradiated ferroelectric thin films. *Appl. Phys. Lett.* **111**, 212905 (2017).
12. El-Saftawy, A. et al. Electron beam induced surface modifications of PET film. *Radiat. Phys. Chem.* **102**, 96–102 (2014).
13. Ding, J. et al. Ultraviolet-irradiated all-organic nanocomposites with polymer dots for high-temperature capacitive energy storage. *Nano-Micro Lett.* **16**, 59 (2024).
14. Zhang, W. et al. Impact of the radiation effect on the energy storage density and wake-up behaviors of antiferroelectric-like Al-doped HfO_2 thin films. *Phys. Chem. Chem. Phys.* **22**, 21893–21899 (2020).
15. Prinzie, J. et al. Low-power electronic technologies for harsh radiation environments. *Nat. Electron.* **4**, 243–253 (2021).
16. Palneedi, H. et al. High-performance dielectric ceramic films for energy storage capacitors: progress and outlook. *Adv. Funct. Mater.* **28**, 1803665 (2018).
17. Croonenborghs, B. et al. X-ray versus gamma irradiation effects on polymers. *Radiat. Phys. Chem.* **76**, 1676–1678 (2007).
18. Clegg, D. et al. *Irradiation Effects on Polymers* (Elsevier, London, New York, 1991).
19. Liu, Y. et al. Flexible ferroelectric $Pb(Zr_{0.53}Ti_{0.47})O_3$ epitaxial films with large radiation and high-temperature tolerance. *Appl. Phys. Lett.* **121**, 122902 (2022).
20. Bastani, Y. et al. Effects of high energy x ray and proton irradiation on lead zirconate titanate thin films' dielectric and piezoelectric response. *Appl. Phys. Lett.* **102**, 192906 (2013).
21. Menou, N. et al. Degradation and recovery of polarization under synchrotron x rays in $SrBi_2Ta_2O_9$ ferroelectric capacitors. *J. Appl. Phys.* **97**, 044106 (2005).
22. Scott, J. F. et al. Radiation effects on ferroelectric thin-film memories: retention failure mechanisms. *J. Appl. Phys.* **66**, 1444–1453 (1989).
23. Ko, Y. J. et al. Flexible $Pb(Zr_{0.52}Ti_{0.48})O_3$ films for a hybrid piezoelectric-pyroelectric nanogenerator under harsh environments. *ACS Appl. Mater. Interfaces* **8**, 6504–6511 (2016).
24. Liu, Y. et al. Radiation-hardened and flexible Pb $(Zr_{0.53}Ti_{0.47})O_3$ piezoelectric sensor for structural health monitoring. *ACS Appl. Mater. Interfaces* **15**, 49362–49369 (2023).
25. Brewer, S. et al. Enhanced radiation tolerance in Mn-doped ferroelectric thin films. *Appl. Phys. Lett.* **111**, 022906 (2017).
26. Cheng, H. et al. Demonstration of ultra-high recyclable energy densities in domain-engineered ferroelectric films. *Nat. Commun.* **8**, 1999 (2017).
27. Shu, L. et al. Partitioning polar-slush strategy in relaxors leads to large energy-storage capability. *Science* **385**, 204–209 (2024).
28. Aramberri, H. et al. Ferroelectric/paraelectric superlattices for energy storage. *Sci. Adv.* **8**, eabn4880 (2022).
29. Nguyen, M. D. et al. Enhancing the energy-storage density and breakdown strength in $PbZrO_3/Pb_{0.9}La_{0.1}Zr_{0.52}Ti_{0.48}O_3$-derived antiferroelectric/relaxor-ferroelectric multilayers. *Adv. Energy Mater.* **12**, 2200517 (2022).
30. Zhang, T. et al. High energy storage performance of opposite double-heterojunction ferroelectricity-insulators. *Adv. Funct. Mater.* **28**, 1706211 (2018).
31. Lu, R. et al. Metadielectrics for high-temperature energy storage capacitors. *Nat. Commun.* **15**, 6596 (2024).
32. Pan, H. et al. Enhanced electric resistivity and dielectric energy storage by vacancy defect complex. *Energy Storage Mater.* **42**, 836–844 (2021).
33. Han, F. et al. High electronic conductivity as the origin of lithium dendrite formation within solid electrolytes. *Nat. Energy* **4**, 187–196 (2019).

34. Lee, Y. W. et al. Dendritic ternary alloy nanocrystals for enhanced electrocatalytic oxidation reactions. *ACS Appl. Mater. Interfaces* **9**, 44018–44026 (2017).
35. Li, X. et al. Dendritic α-Fe_2O_3/TiO_2 nanocomposites with improved visible light photocatalytic activity. *Phys. Chem. Chem. Phys.* **18**, 9176–9185 (2016).
36. Zasadzińska, M. et al. Investigation of the dendritic structure influence on the electrical and mechanical properties diversification of the continuously casted copper strand. *Materials* **13**, 5513 (2020).
37. MacManus-Driscoll, J. L. Self-assembled heteroepitaxial oxide nanocomposite thin film structures: designing interface-induced functionality in electronic materials. *Adv. Funct. Mater.* **20**, 2035–2045 (2010).
38. Liu, W. et al. Tutorial review on structure–dendrite growth relations in metal battery anode supports. *Chem. Soc. Rev.* **49**, 7284–7300 (2020).
39. Jayakrishnan, A. et al. Are lead-free relaxor ferroelectric materials the most promising candidates for energy storage capacitors? *Prog. Mater. Sci.* **132**, 101046 (2023).
40. Balaraman, A. A. et al. Inorganic dielectric materials for energy storage applications: a review. *J. Phys. D. Appl. Phys.* **55**, 183002 (2022).
41. Jayakrishnan, A. R. et al. Recent development of lead-free relaxor ferroelectric and antiferroelectric thin films as energy storage dielectric capacitors. *J. Eur. Ceram. Soc.* **44**, 4332–4349 (2024).
42. Zhang, L. Understanding the radiation resistance mechanisms of nanocrystalline metals from atomistic simulation. *Metals* **11**, 1875 (2021).
43. Ackland, G. Controlling radiation damage. *Science* **327**, 1587–1588 (2010).
44. Beyerlein, I. et al. Radiation damage tolerant nanomaterials. *Mater. Today* **16**, 443–449 (2013).
45. Trefilova, L. N. et al. Role of sodium in radiation defect formation in CsI crystals. *Radiat. Meas.* **33**, 687–692 (2001).
46. Shrout, T. R. et al. Lead-free piezoelectric ceramics: alternatives for PZT? *J. Electroceram.* **19**, 113–126 (2007).
47. Wang, P. et al. High-temperature flexible nanocomposites with ultra-high energy storage density by nanostructured MgO fillers. *Adv. Funct. Mater.* **32**, 2204155 (2022).
48. Jafarova, V. et al. Structural and electronic properties of ZnO: a first-principles density-functional theory study within LDA (GGA) and LDA (GGA)+ U methods. *Solid State Commun.* **325**, 114166 (2021).
49. Yang, M. et al. Polymer nanocomposite dielectrics for capacitive energy storage. *Nat. Nanotechnol.* **19**, 588–603 (2024).
50. Kobayashi, R. Modeling and numerical simulations of dendritic crystal growth. *Phys. D.* **63**, 410–423 (1993).
51. Juan, T. P. et al. Temperature dependence of the current conduction mechanisms in ferroelectric $Pb(Zr_{0.53}, Ti_{0.47})O_3$ thin films. *J. Appl. Phys.* **95**, 3120–3125 (2004).
52. Warren, W. et al. Identification of paramagnetic Pb^{+3} defects in lead zirconate titanate ceramics. *Appl. Phys. Lett.* **62**, 482–484 (1993).
53. Li, W. et al. Vertical-interface-manipulated conduction behavior in nanocomposite oxide thin films. *ACS Appl. Mater. Interfaces* **6**, 5356–5361 (2014).
54. Li, W. et al. Nanostructure manipulation and its influence on functionalities in self-assembled oxide thin films. *J. Appl. Phys.* **116**, 183904 (2014).
55. Li, W. et al. Defects in complex oxide thin films for electronics and energy applications: challenges and opportunities. *Mater. Horiz.* **7**, 2832–2859 (2020).
56. Chen, A. et al. Metal oxide nanocomposites: a perspective from strain, defect, and interface. *Adv. Mater.* **31**, 1803241 (2019).
57. Liu, B. et al. Neutron radiation effects in $Bi_{3.15}Nd_{0.85}Ti_3O_{12}$ ferroelectric thin film capacitors. *Radiat. Eff. Defect. Solids* **168**, 115–120 (2013).
58. Giegerich, U. et al. The stability of ferroelectric polarization of PVDF upon irradiation. *IEEE T. Dielect. El. In.* **7**, 353–359 (2000).
59. Seshadri, S. B. et al. Unexpectedly high piezoelectricity of Sm-doped lead zirconate titanate in the Curie point region. *Sci. Rep.* **8**, 4120 (2018).
60. Oikawa, T. et al. Composition and orientation dependence of electrical properties of epitaxial $Pb(Zr_xTi_{1-x})O_3$ thin films grown using metalorganic chemical vapor deposition. *J. Appl. Phys.* **95**, 3111–3115 (2004).
61. Boucher, E. et al. Effect of (Mn, F) and (Mg, F) co-doping on dielectric and piezoelectric properties of lead zirconate titanate ceramics. *J. Appl. Phys.* **92**, 5437–5442 (2002).
62. Leray, J.-L. et al. Radiation effects in thin-film ferroelectric PZT for non-volatile memory applications in microelectronics. *J. Phys. III* **7**, 1227–1243 (1997).
63. Claeys, C. et al. *Radiation Effects in Advanced Semiconductor Materials and Devices* (Springer Science & Business Media, 2013).
64. Li, W. et al. Manipulating multiple order parameters via oxygen vacancies: the case of $Eu_{0.5}Ba_{0.5}TiO_{3-\delta}$. *Phys. Rev. B* **96**, 115105 (2017).
65. Saremi, S. et al. Enhanced electrical resistivity and properties via ion bombardment of ferroelectric thin films. *Adv. Mater.* **28**, 10750–10756 (2016).
66. Nguyen, M. D. et al. Relaxor-ferroelectric thin film heterostructure with large imprint for high energy-storage performance at low operating voltage. *Energy Storage Mater.* **25**, 193–201 (2020).
67. Sun, Y. et al. Ultrahigh energy storage density in glassy ferroelectric thin films under low electric field. *Adv. Sci.* **9**, 2203926 (2022).
68. Cheema, S. S. et al. Giant energy storage and power density negative capacitance superlattices. *Nature* **629**, 803–809 (2024).
69. Hoffmann, M. et al. Negative capacitance for electrostatic supercapacitors. *Adv. Energy Mater.* **9**, 1901154 (2019).
70. Shen, Z. H. et al. High-throughput phase-field design of high-energy-density polymer nanocomposites. *Adv. Mater.* **30**, 1704380 (2018).
71. Wang, J. et al. Phase transitions and domain structures of ferroelectric nanoparticles: phase field model incorporating strong elastic and dielectric inhomogeneity. *Acta Mater.* **61**, 7591–7603 (2013).
72. Chen, L.-Q. Phase-field models for microstructure evolution. *Annu. Rev. Mater. Res.* **32**, 113–140 (2002).
73. Chen, L. Q. et al. Applications of semi-implicit Fourier-spectral method to phase field equations. *Comput. Phys. Commun.* **108**, 147–158 (1998).
74. Chen, L.-Q. APPENDIX A–Landau free-energy coefficients. In *Physics of Ferroelectrics: A Modern Perspective* (eds Rabe, K. M., Ahn, C. H., & Triscone, J.-M.) 363–372 (Springer, 2007).
75. Haun, M. et al. Thermodynamic theory of the lead zirconate-titanate solid solution system, part I: phenomenology. *Ferroelectrics* **99**, 13–25 (1989).
76. Li, Y. et al. Effect of substrate constraint on the stability and evolution of ferroelectric domain structures in thin films. *Acta Mater.* **50**, 395–411 (2002).
77. Li, Y. et al. Effect of electrical boundary conditions on ferroelectric domain structures in thin films. *Appl. Phys. Lett.* **81**, 427–429 (2002).

Acknowledgements

This work was supported by the Basic Science Center Project of the National Natural Science Foundation of China (NSFC) grant 52388201 (C.-W.N.); the National Natural Science Foundation of China (NSFC) grants 92477107 (W.-W.L.), 52102177 (W.-W.L.), 52472125 (J.W.), 52302184 (Y.Z.), 52403297 (M.L.), and 12275130 (P.G.); the Research Fund for Stable Support for Basic Research Projects of National

Defense Characteristics grant ILF240031A24 (W.-W.L.); the Research Fund of State Key Laboratory of Mechanics and Control for Aerospace Structures (Nanjing University of Aeronautics and Astronautics) grant MCAS-I-0424G02 (W.-W.L.); the Research Fund of State Key Laboratory of New Ceramic and Fine Processing (Tsinghua University) grant No. KF202308 (Y.Z.); the National Natural Science Foundation of Jiangsu Province grant BK20241426 (M.L.), and Young Elite Scientists Sponsorship Program of Jiangsu Association for Science and Technology grant No. JSTJ–2024-010 (M.L.); Top-notch Academic Programs Project of Jiangsu Higher Education Institutions (TAPP) (W.-W.L.), and the Jiangsu Specially-Appointed Professor Program (W.-W.L.). Y.Z. also acknowledges Beijng PARATERA Tech CO.,Ltd. for providing HPC resources that have contributed to the research results reported within this paper (URL: https://www.paratera.com/).

Author contributions

W.-W.L. conceived and supervised this study; Y.L. performed the experiments with the supervision of W.-W.L. and J.W.; Y.Z. performed the phase-field simulations; Y.L. fabricated the samples and carried the electrical measurements with the help from J.W., K.J., P.G., S.S., D.L., H.L., X.H.; M.L. performed the STEM measurements; Y.L., Y.Z., J.W., W.-W.L., and C.-W.N. wrote the draft of the manuscript. All authors discussed the results and revised the manuscript.

Competing interests

The authors declare no competing interests.

Additional information

Supplementary information The online version contains supplementary material available at https://doi.org/10.1038/s41467-025-59225-z.

Correspondence and requests for materials should be addressed to Yang Zhang, Jing Wang, Weiwei Li or Ce-Wen Nan.

Peer review information *Nature Communications* thanks Aditi Sahoo, Ampattu R. Jayakrishnan, and the other, anonymous, reviewer(s) for their contribution to the peer review of this work. A peer review file is available.